Journal of Quantitative Spectroscopy & Radiative Transfer 105 (2007) 32–54

Journal of Quantitative Spectroscopy & Radiative Transfer

www.elsevier.com/locate/jqsrt

One-dimensional solar radiative transfer: Perturbation approach and its application to independent-pixel calculations for realistic cloud fields

Matthias Jerg[a,b,*], Thomas Trautmann[b]

[a]*Institute for Meteorology, University of Leipzig, Stephanstrasse 3, 04103 Leipzig, Germany*

[b]*Remote Sensing Technology Institute, German Aerospace Center (DLR), IMF, Münchner Straße 20, P.O. Box 1116, 82234 Weßling, Germany*

Received 3 July 2006; received in revised form 20 September 2006; accepted 21 September 2006

Abstract

The radiative transfer perturbation theory (RTPT), which has already been introduced in atmospheric radiative transfer several years ago, is applied to cloud related problems. The RTPT requires the solution of the radiative transfer equation in the forward and the adjoint mode. The basic principles of this technique are presented as well as its extensions to isotropic surface reflection and its conjunction with the Hermite interpolation. This set of methods is applied to different atmospheric conditions including realistic cloud scenes. The results are compared with the usual (forward) independent-pixel calculations with respect to errors of individual pixels and domain-averaged values. The RTPT turns out to be sufficiently accurate in the case the clouds' internal vertical variations remain moderate. It is also shown that, depending on the specific radiative transfer problem, the RTPT can offer some advantages on computational speed. However, the limitations of the RTPT with regard to realistic clouds are addressed as well.

Keywords: Radiative transfer; Perturbation theory; Independent-pixel; Clouds; DISORT

1. Introduction

In this paper, we present the radiative transfer perturbation theory (RTPT) in the context of independent-pixel calculations. The technique originally stems from mathematically related topics such as neutron transport, see [1] and has been introduced to atmospheric radiation problems several years ago by Marchuk [2] and Box et al. [3]. With this method it is necessary to compute a base case which corresponds to a certain condition of the optical parameters of the atmosphere. Small deviations from this base case can then be taken into account mainly by integration over the result of the base case. More recently, the work carried out by Gabriel et al. [4] achieves the direct implementation of the RTPT in a two-stream model. In a following paper,

*Corresponding author. Institute for Meteorology, University of Leipzig, Stephanstrasse 3, 04103 Leipzig, Germany. Tel.: +8153 28 2683; fax: +8153 28 1446.

E-mail addresses: matthias.jerg@dlr.de (M. Jerg), thomas.trautmann@dlr.de (T. Trautmann).

0022-4073/$ - see front matter © 2006 Elsevier Ltd. All rights reserved.
doi:10.1016/j.jqsrt.2006.09.014

see [5], this implementation is applied to broadband radiative transfer calculations in order to accelerate radiative transfer calculations in independent-pixel mode. In the paper here, a similar aim is pursued by embedding the RTPT in a multi-stream radiative transfer model. A way to deal with considerable deviations, which would usually be beyond the range of application of the linear perturbation theory, is also presented. This is achieved simply by dealing with several base cases and thereafter interpolating between these base cases by means of the Hermite interpolation. This extension is applied to stand-alone problems as well as to realistic cloud scenes. While the former are used to investigate the overall applicability and features of the method, the latter aims at the investigation of the potential the method has to accelerate independent pixel calculations. All radiative transfer calculations have been carried out by the model DISORT, see [6].

2. Forward and adjoint formulation of the transport problem

Following [3] and adopting these authors' notation for a plane-parallel atmosphere, the radiative transfer equation in operator notation reads

$$LI(z,\vec{\Omega}) = Q(z,\vec{\Omega}), \tag{1}$$

where L is the transport operator, I is the intensity field and Q is the source of radiation. The vector $\vec{\Omega} = (\theta, \phi)$ represents the direction of travel of the photons. The transport operator L may be written here as

$$L \coloneqq \mu \frac{\partial}{\partial z} + \sigma_t(z) - \frac{\sigma_s(z)}{4\pi} \int_{4\pi} d\Omega'\, p(z,\vec{\Omega}',\vec{\Omega})\ \circ. \tag{2}$$

The symbol "$\circ$" implies that the intensity I has to be included in the integration. The optical properties of the atmosphere are the scattering coefficient σ_s, the absorption coefficient σ_a, the extinction coefficient $\sigma_t = \sigma_s + \sigma_a$ and the scattering phase function p. μ is the cosine of the zenith angle θ.

For solar radiative transfer, which is dealt with in this paper exclusively, the source function can be written as

$$Q \coloneqq |\mu_\odot| F_\odot \delta(\mu - \mu_\odot)\delta(\phi - \phi_\odot)\delta(z - z_{TOA}) \tag{3}$$

with $\mu_\odot$ being the cosine of the solar illumination here given as flux $F_\odot$, $\phi_\odot$ the azimuthal direction of the sun and z_{TOA} the altitude of the upper boundary of the model atmosphere. Eq. (1) has to fulfill the following vacuum boundary conditions:

$$I(z = 0, \vec{\Omega} > 0) = 0, \tag{4}$$

$$I(z = TOA, \vec{\Omega} < 0) = 0 \tag{5}$$

meaning that no additional diffuse radiation enters the medium from top or bottom. For the following it is convenient to introduce the definition of the inner product of two functions F_1, F_2 as

$$\langle F_1, F_2 \rangle \coloneqq \int_0^{TOA} \int_0^{2\pi} \int_{-1}^{1} F_1 F_2 \, d\mu \, d\phi \, dz. \tag{6}$$

After introducing a second set of functions $\{I^+(z,\vec{\Omega})\}$, it is possible to define the so-called adjoint transport operator L^+ by the relation:

$$\langle I^+, LI \rangle = \langle L^+ I^+, I \rangle. \tag{7}$$

After postulating the following form of the adjoint transport operator:

$$L^+ \coloneqq -\mu \frac{\partial}{\partial z} + \sigma_t(z) - \frac{\sigma_s(z)}{4\pi} \int_{4\pi} d\Omega'\, p(z,\vec{\Omega}',\vec{\Omega}) \circ \tag{8}$$

it can be shown that the boundary conditions must result in:

$$I^+(z = TOA, \vec{\Omega} > 0) = 0, \tag{9}$$

$$I^+(z = 0, \vec{\Omega} < 0) = 0 \tag{10}$$

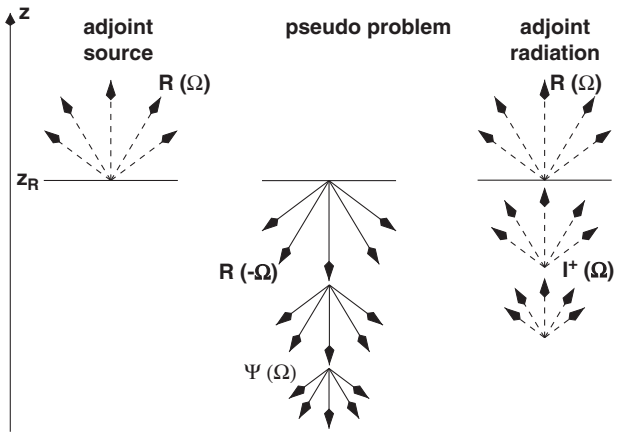

Fig. 1. Explanation of the adjoint radiance field.

meaning no adjoint radiance leaves the medium at the upper and lower boundary. An illustration of this physically unusual behavior of the adjoint photons is given below. After this formal introduction the boundary conditions and the adjoint transport operator constitute together with a so far arbitrary adjoint source $Q^+(z,\vec{\Omega})$ the adjoint transport equation:

$$L^+I^+(z,\vec{\Omega}) = Q^+(z,\vec{\Omega}). \tag{11}$$

One might think that the solution of Eq. (11) requires the design of a new computer code. However, that is not the case as, according to [3], Eq. (11) can be transformed into a pseudo problem:

$$L\Psi = Q^+(z,-\vec{\Omega}) \tag{12}$$

by introducing

$$I^+(z,\vec{\Omega}) = \Psi(z,-\vec{\Omega}). \tag{13}$$

That means, in order to derive the adjoint radiance field, one has to solve the forward equation with the adjoint source having its angular dependence swapped and the forward boundary conditions applied. For the comfort of the reader the steps leading to Eq. (12) are presented and commented on in Appendix A. This derivation of I^+ might be valuable as [5] pointed out that the direct formulation and solution of Eq. (11) can lead to unstable solutions where the transmission and reflection can exceed unity in a strongly absorbing medium, see also below.

With this pseudo description of the adjoint radiance, it is possible to achieve a better insight in the behavior of the adjoint photons. In anticipation of the beginning of the next paragraph consider as effect of interest the upwelling flux at position z_R, see Fig. 1. That means the response function R reads as in Eq. (15). The method illustrated by the pseudo problem then implies to swap the source (response) function with respect to angles, meaning that the adjoint source radiates downward. Therefore, the pseudointensity field Ψ would also be directed downward (neglecting scattering in this illustration). Eq. (13) then rules to swap the direction of propagation of this field as well, resulting in an adjoint radiance field that points upward to an upward illuminating source.

3. Perturbation theory

In many cases one is not interested in the intensity field itself, but rather in quantities deduced from the intensity field. Both can be described in general as radiative effect E. The formal extraction of this effect from the intensity field can be achieved by the introduction of the response function R. Its insertion together with

I in Eq. (6) yields

$$E := \int_0^{TOA} \int_{-1}^{1} \int_0^{2\pi} R\, I \, \mathrm{d}\phi \, \mathrm{d}\mu \, \mathrm{d}z = \langle R, I \rangle. \tag{14}$$

For example, if one is interested in the upwelling flux at position z_R, R would be

$$R(z, \mu) = \mu \eta(\mu) \delta(z - z_R) \tag{15}$$

with

$$\eta(\mu) = \begin{cases} 1, & 0 \leqslant \mu \leqslant 1, \\ 0, & -1 \leqslant \mu < 1. \end{cases} \tag{16}$$

To obtain the radiative effect usually one would compute the intensity field by solving Eq. (1) and then proceed with Eq. (14). An alternative way is also possible if the response function R for the desired effect is chosen as adjoint source in Eq. (11). One can then rewrite the adjoint transport equation as

$$L^+ I^+(z, \vec{\Omega}) = R(z, \vec{\Omega}) \tag{17}$$

and with relation (7) it becomes obvious that the effect has two equal representations:

$$E = \langle R, I \rangle \equiv \langle I^+, Q \rangle. \tag{18}$$

Suppose now the state of the atmosphere and its optical parameters can be separated in a so-called base case and in the perturbations from this base case:

$$\sigma_\mathrm{s}(z) = \sigma_{\mathrm{s,b}}(z) + \Delta\sigma_\mathrm{s}(z), \tag{19}$$

$$\sigma_\mathrm{a}(z) = \sigma_{\mathrm{a,b}}(z) + \Delta\sigma_\mathrm{a}(z), \tag{20}$$

$$\chi_l(z) = \chi_{l,\mathrm{b}}(z) + \Delta\chi_l(z), \tag{21}$$

where χ_l is the Legendre expansion coefficient of order l of the phase function. The transport operator then becomes

$$L(z, \vec{\Omega}) = L_\mathrm{b}(z, \vec{\Omega}) + \Delta L(z, \vec{\Omega}), \tag{22}$$

$$L^+(z, \vec{\Omega}) = L_\mathrm{b}^+(z, \vec{\Omega}) + \Delta L^+(z, \vec{\Omega}), \tag{23}$$

where b and Δ denote the base case and the perturbation, respectively.

Given the transport equations are solved with respect to the base case for a chosen effect, meaning one has to solve

$$L_\mathrm{b} I_\mathrm{b} = Q, \tag{24}$$

$$L_\mathrm{b}^+ I_\mathrm{b}^+ = R \tag{25}$$

the intensities also split up to

$$I(z, \vec{\Omega}) = I_\mathrm{b}(z, \vec{\Omega}) + \Delta I(z, \vec{\Omega}), \tag{26}$$

$$I^+(z, \vec{\Omega}) = I_\mathrm{b}^+(z, \vec{\Omega}) + \Delta I^+(z, \vec{\Omega}). \tag{27}$$

If we now use these separations of the intensities and the transport operators in the definition of the effect, Eq. (14), we can expand the effect in a series where second order terms are neglected. However, [7] offers a more formal way to derive the perturbation series which also includes the perturbation of the source. Appendix B presents its main steps. If the perturbation of the source is neglected, the linear perturbation series reads

$$E = E_\mathrm{b} - \Delta E = \langle I_\mathrm{b}, R \rangle - \langle I_\mathrm{b}^+, \Delta L I_\mathrm{b} \rangle \equiv \langle I_\mathrm{b}^+, Q \rangle - \langle I_\mathrm{b}^+, \Delta L I_\mathrm{b} \rangle. \tag{28}$$

There are several notable facts about Eq. (28). As mentioned above, one has to recognize that E_b has two equivalent representations which directly transform into one another by means of relation (7). The representation

$$E_\mathrm{b} = \langle I_\mathrm{b}, R \rangle \tag{29}$$

is the common definition of the effect. Here, one has to calculate I_b for one solar cosine $\mu_\odot$ and gains I_b usually at all levels of the atmosphere. For a second solar cosine one has to repeat the entire calculation. Opposed to this representation, the expression

$$E_b = \langle I_b^+, Q \rangle \tag{30}$$

has the advantage that the calculation of I_b^+ is independent of the solar cosine. The actual value of $\mu_\odot$ is chosen by the integration over the source Q. On the other hand, the result for I_b^+ was derived with a special position z_R according to the assignment of a special response function R. Therefore, both approaches to E are somewhat complementary and their respective usage is subject to the problem at hand. Moreover, the potentially unstable behavior of the adjoint solution, which was mentioned above, was investigated by numerical experiments. With the help of Eq. (30), solutions for transmission and reflection can be derived via the calculation of I^+ by means of the pseudo problem represented by Eq. (12). In the first experiment, the parameters $\tau = 10$ and $\omega_o = 0.0$ and $\mu_\odot = 0.7$ for a homogeneous column were used. The result was: $T = 6.249 \times 10^{-7}$ and $R = 0.0$. For the second experiment $\tau = 10$, $\omega_o = 0.5$, and a Henyey–Greenstein phase function with $g = 0.75$ was employed. The solar illumination was maintained. $T = 3.242 \times 10^{-4}$ and $R = 2.798 \times 10^{-2}$ was derived. These results have been confirmed by calculations of T and R in the usual manner directly by Eq. (29). For the definition of T and R see relation (55). As a result, the derivation of I^+ via the pseudo problem, and thus the perturbation integral, can be considered unconditionally stable.

Another interesting feature of Eq. (28) is that the perturbation integral $\langle I_b^+, \Delta L I_b \rangle$ contains only results with respect to the base case optical properties. That means, that starting from a base case the influence of small (in the linear sense) perturbations of this base case can be calculated in a brief manner by the integral over the phase space spanned by the variables z, μ, ϕ.

In the following, we will limit ourselves to azimuthally independent effects such as fluxes. The appropriate form of ΔE after expanding the phase function in a series of Legendre polynomials can be found in [8]:

$$\Delta E(z_R) = 2\pi \int_0^{TOA} \mathrm{d}z \left(\Delta\sigma_t(z)\Xi(z) - \frac{1}{2}\sum_{l=0}^{\infty}(2l+1)\Delta\eta_l(z)\xi_l^+(z)\xi_l(z) \right), \tag{31}$$

where

$$\bar{I}_b(z,\mu) = \frac{1}{2\pi}\int_0^{2\pi} \mathrm{d}\mu\, I_b(z,\mu,\phi), \tag{32}$$

$$\Xi(z) = \int_{-1}^{1} \mathrm{d}\mu\, \bar{I}_b^+(z,\mu)\bar{I}_b(z,\mu), \tag{33}$$

$$\xi_l(z) = \int_{-1}^{1} \mathrm{d}\mu\, \bar{I}_b(z,\mu)P_l(\mu), \tag{34}$$

$$\xi_l^+(z) = \int_{-1}^{1} \mathrm{d}\mu\, \bar{I}_b^+(z,\mu)P_l(\mu) \tag{35}$$

and

$$\Delta\eta_l(z) = \eta_l(z) - \eta_{l,b}(z) = \Delta\sigma_s(z)\chi_{l,b}(z) + \sigma_{s,b}\Delta\chi_l(z). \tag{36}$$

If Eq. (31) is further split up according to the physical meaning of its components, one yields

$$\mathscr{D}_{s,e}(z_R) = 2\pi \int_0^{TOA} \Delta\sigma_s(z)\Xi(z)\,\mathrm{d}z, \tag{37}$$

$$\mathscr{D}_{s,is}(z_R) = -\pi \int_0^{TOA} \sum_{l=0}^{\infty}(2l+1)\Delta\sigma_s\chi_{l,b}(z)\xi_l^+(z)\xi_l(z)\,\mathrm{d}z, \tag{38}$$

$$\mathscr{D}_{\mathrm{a},e}(z_R) = 2\pi \int_0^{TOA} \Delta\sigma_{\mathrm{a}}(z)\Xi(z)\,\mathrm{d}z, \tag{39}$$

$$\mathscr{D}_p(z_R) = -\pi \int_0^{TOA} \sum_{l=0}^{\infty}(2l+1)\Delta\chi_l\sigma_{\mathrm{s},b}(z)\xi_l^+(z)\xi_l(z)\,\mathrm{d}z. \tag{40}$$

A couple of remarks might be useful at this point. It has to be pointed out that all sorts of perturbations can be dealt with this description of the perturbation integral. The components of the integral as stated in Eqs. (37)–(40) directly relate to the different perturbations. Eq. (37) describes the scattering contribution of changes in the extinction coefficient, Eq. (38) describes the inscattering contribution of the scattering coefficient, Eq. (39) is responsible for the influence of changes in the absorption coefficient which contribute to the extinction and finally Eq. (40) describes the effect originating from changes in the phase function coefficients. The first three components are considered to change the total optical depth of the medium, which will be important at some later stage. Even more, by comparison with the *Taylor Series*, the components of the perturbation integral can be directly linked to the derivative of the respective atmospheric property, see for example [9].

4. Incorporation of surface reflection

To this point, every formula deduced was related to vacuum boundary conditions. In order to include reflection at the lower boundary, one can pursue two different approaches. First, it is of course possible to directly include the lower boundary condition in the solution for the base case. This means, one has to change the system of equations the radiative transfer model uses. That further implies that the surface albedo would become part of the base case calculation. As in our case, the goal is to use the RTPT for independent-pixel calculations it would require all pixels to have the same albedo. That is a restriction we want to avoid, however, we limit ourselves to isotropic (Lambertian) surface reflection. Thus, we cannot follow the approach above as this would result in the computation of a base case for nearly each pixel and would therefore make no sense within the concept and the aims of the perturbation approach. The other method left to pursue is to use a superposition of the vacuum results and some additional computation that accounts for the surface reflection. This approach has already been described in the context of the perturbation theory by Box et al. [3] and in a more general fashion by Landgraf et al. [10]. Its formal derivation has been recently readdressed by Muldashev et al. [11]. However, for the sake of continuity we follow here [3]. As shown by Liou [12], the influence of a Lambertian surface with albedo A can be written as

$$I(z,\vec{\Omega}) = I_{\mathrm{v}}(z,\vec{\Omega}) + F_{\mathrm{v}}(z=0)\frac{A}{1-A\bar{s}}I_{\mathrm{s}}(z,\vec{\Omega}), \tag{41}$$

where I_{v} is the intensity derived with respect to vacuum boundary conditions and the flux:

$$F_{\mathrm{v}}(z=0) = \frac{1}{\pi}\int_0^{2\pi}\mathrm{d}\phi\int_{-1}^{0}\mathrm{d}\mu\,|\mu| I_{\mathrm{v}}(z=0,\vec{\Omega}). \tag{42}$$

Another flux, also derived with respect to vacuum boundary conditions, is

$$\bar{s} = \frac{1}{\pi}\int_0^{2\pi}\mathrm{d}\phi\int_{-1}^{0}\mathrm{d}\mu\,|\mu| I_{\mathrm{s}}(z=0,\vec{\Omega}) \tag{43}$$

with I_{s} being the solution of the special radiative transfer problem:

$$LI_{\mathrm{s}} = Q_{\mathrm{s}} \tag{44}$$

with source Q_{s}:

$$Q_{\mathrm{s}} = \mu\eta(\mu)\delta(z) \tag{45}$$

which establishes an isotropic source at the lower boundary of the medium which radiates upward. For reciprocity reasons the formula for the adjoint radiance becomes

$$I^+(z,\vec{\Omega}) = I_{\mathrm{v}}^+(z,\vec{\Omega}) + F_{\mathrm{v}}^+(z=0)\frac{A}{1-A\bar{s}} I_{\mathrm{s}}(z,-\vec{\Omega}), \tag{46}$$

where

$$F_{\mathrm{v}}^+(z=0) = \frac{1}{\pi}\int_0^{2\pi} \mathrm{d}\phi \int_0^1 \mathrm{d}\mu\, |\mu| I_{\mathrm{v}}^+(z=0,\vec{\Omega}). \tag{47}$$

Eqs. (41) and (46) are now inserted in Eq. (31). The following somewhat lengthy but straightforward calculation is omitted and only the result will be give here as

$$E = E_{\mathrm{b}} - \Delta E = E_{\mathrm{b,v}} + E_{\mathrm{b,a}} - \Delta E_{\mathrm{v}} - \Delta E_{\mathrm{a}} \tag{48}$$

with $E_{\mathrm{b,v}}$ and ΔE_{v} as given in Eqs. (28) and (31), respectively. The remaining two terms, which provide for the albedo effect are

$$E_{\mathrm{b,a}} = 2\pi\mathscr{A} F_{\mathrm{v,b}}(0) \int_0^{TOA}\int_{-1}^1 \mathrm{d}\mu\, \mathrm{d}z R I_{\mathrm{s,b}}(z,\mu), \tag{49}$$

$$\Delta E_{\mathrm{a}} = 2\pi\mathscr{A}\int_0^{TOA} \mathrm{d}z \Bigg\{ \Delta\sigma_{\mathrm{t}}(z)\left(\mathscr{F}_1(z) + \mathscr{F}_2(z) + \mathscr{A}\mathscr{F}_3(z)\right) - \frac{1}{2}\sum_{l=0}^{\infty}(2l+1)\Delta\eta_l(z)\left(\mathscr{F}_{\xi_1}(z) + \mathscr{F}_{\xi_2}(z) + \mathscr{A}\mathscr{F}_{\xi_3}(z)\right)\Bigg\}, \tag{50}$$

where

$$\mathscr{A} = \frac{A}{1-A\bar{s}_{\mathrm{b,v}}}, \tag{51}$$

$$\begin{aligned}
&\mathscr{F}_1(z) = F_{\mathrm{v,b}}(0)\Xi_1(z), \quad \mathscr{F}_{\xi_1}(z) = \Xi_{\xi_1}(z)F_{\mathrm{v,b}}(0),\\
&\mathscr{F}_2(z) = F_{\mathrm{v,b}}^+(0)\Xi_2(z), \quad \mathscr{F}_{\xi_2}(z) = \Xi_{\xi_2}(z)F_{\mathrm{v,b}}^+(0),\\
&\mathscr{F}_3(z) = F_{\mathrm{v,b}}(0)F_{\mathrm{v,b}}^+(0)\Xi_{\mathrm{s}}(z), \quad \mathscr{F}_{\xi_3}(z) = F_{\mathrm{v,b}}(0)F_{\mathrm{v,b}}^+(0)\Xi_{\xi_3}(z),
\end{aligned}$$

$$\begin{aligned}
&\Xi_1(z) = \int_{-1}^1 \mathrm{d}\mu\, I_{\mathrm{v,b}}^+(z,\mu) I_{\mathrm{s,b}}(z,\mu), \quad \Xi_{\xi_1}(z) = \xi_{l,\mathrm{v}}^+(z)\xi_{l,\mathrm{s}}(z),\\
&\Xi_2(z) = \int_{-1}^1 \mathrm{d}\mu\, I_{\mathrm{s,b}}(z,-\mu)\bar{I}_{\mathrm{b,v}}(z,\mu), \quad \Xi_{\xi_2}(z) = \xi_{l,\mathrm{s}}^+(z)\xi_{l,\mathrm{v}}(z),\\
&\Xi_{\mathrm{s}}(z) = \int_{-1}^1 \mathrm{d}\mu\, I_{\mathrm{s,b}}(z,-\mu) I_{\mathrm{s,b}}(z,\mu), \quad \Xi_{\xi_3}(z) = \xi_{l,\mathrm{s}}^+(z)\xi_{l,\mathrm{s}}(z),\\
&\xi_{l,\mathrm{s}}(z) = \int_{-1}^1 \mathrm{d}\mu\, I_{\mathrm{s,b}}(z,\mu) P_l(\mu), \quad \xi_{l,\mathrm{s}}^+(z) = \int_{-1}^1 \mathrm{d}\mu\, I_{\mathrm{s,b}}(z,-\mu) P_l(\mu),
\end{aligned}$$

$$\Delta\eta_l(z) = \Delta\sigma_{\mathrm{s}}(z)\chi_{l,\mathrm{b}}(z) + \Delta\chi_l(z)\sigma_{\mathrm{s,b}}(z). \tag{52}$$

In the above relations the subscript "v" means "derived with respect to vacuum boundary conditions" and the subscript "b" means "derived with respect to base case optical properties", combinations accordingly. It can

be concluded that, analogously to Eq. (31), all integrals are deduced with respect to vacuum boundary conditions and/or base case optical properties. The latter is also true for the results of the special source function problem, denoted with subscript "s". Therefore, the flexibility which was demanded in the first paragraph of this section is fulfilled. Noteworthy in this respect is also the fact that if one has chosen the downwelling flux as sought-after effect the solution for problem (44) is already included in the adjoint radiance field as a subset and no further radiative transfer calculation is necessary.

5. Interpolation technique

With the last paragraph we have everything ready to apply the RTPT to atmospheric problems. However, before results for the linear perturbation theory will be shown, a significant but simple extension will be introduced. As pointed out before, we can expect the linear RTPT to match exact calculations with sufficient accuracy only in a narrow interval around the base case. Similar to the application of the Taylor series, beyond this range errors can become quite large. To remedy this problem to some extent we will make use of the so-called Hermite interpolation whose basic principles can be found in [13,14]. This method stands out to some extent by the circumstance that it uses not only the value of a function at discrete nodes but also its derivative. This fact makes it valuable for the perturbation theory as the first order derivatives are here provided in a direct and analytic manner, see Section 4. In order to extend the range of application of the RTPT in regard to changes in the optical depth, two (or more) bases-cases which differ by their total optical depth are computed, and the total optical depth τ_t is used as interpolation parameter. According to the above cited literature the third order interpolation formula for an interval confined by the two total optical depths τ_0 and τ_1 is

$$\begin{aligned} E(\tau_t, z) = {} & E_0(\tau_0, z)(1 - 3s^2 + 2s^3) + E_1(\tau_1, z)(3s^2 - 2s^3) \\ & + \Delta E_0(\tau_0, z)(s - 2s^2 + s^3) + \Delta E_1(\tau_1, z)(s^3 - s^2), \end{aligned} \tag{53}$$

where

$$s = \frac{\tau_t - \tau_0}{\tau_1 - \tau_0}. \tag{54}$$

E_0 and E_1 are the effects, and finally ΔE_0, ΔE_1 are the perturbation integrals which refer to changes of the total optical depth. Although the interpolation parameter s is derived from the total optical depth of the whole column, Eq. (53) is also applied at internal layer interfaces by employing the respective perturbation integrals of these positions. This implies that the technique can be successfully applied if the columns treated by Eq. (53) are closely related to the base case columns in terms of the vertical distribution of the optical parameters. Ideally, all columns can be transferred into each other by a simple scaling while the cloud top and base has no horizontal variation. However, studies show that even for vertically inhomogeneous perturbations meaningful results are gained, see below. This point will also be re-addressed when discussing the independent-pixel applications. The phase function perturbation is unaltered added linearly to Eq. (53).

6. Applications and results

In the following sections, the perturbation theory will be applied to a number of atmospheric conditions all related to clouds one way or another. In the first part, the linear perturbation theory and the Hermite interpolation will be employed as stand-alone methods to compute alterations of one atmospheric column. In the second part, results for the Hermite interpolation will be shown when utilized to compute realistic cloud scenes. As mentioned before, the adjoint calculation, the perturbation theory, and the Hermite interpolation have been embedded in and built around the radiative transfer model DISORT. DISORT has also been used to perform the exact (benchmark) calculations. For all calculations four computational polar angles (NSTR) have been used. Therefore, the infinite summation in Eq. (31) can be truncated for terms l larger than NSTR-1. Note that for simplicity in all calculations an incoming solar flux $F_\odot$ equal to one was used.

6.1. Perturbation theory and interpolation

In order to show the overall capabilities of the linear perturbation theory as well as its limitations in this section, two different cases of atmospheric perturbations will be shown.

6.1.1. Perturbation of the extinction/scattering coefficient

In this example, see Fig. 2, the scattering coefficient is perturbed while the absorption coefficient is set to zero. The base case is constant with height, $\sigma_t = \sigma_s = 0.005\,m^{-1}$, thus composing an atmosphere of optical depth of 10. The scattering coefficient is then altered in 10 steps, increasing by 5% per step below 500 m and above 1500 m, and by 10% per step in the intermediate interval. All relative values refer to the original base case value. Hence, any unrealistic values for optical properties are avoided. The different perturbation steps are shown in Fig. 2 as dashed lines. The scattering phase function, here chosen to be the Henyey–Greenstein-type with asymmetry parameter $g = 0.75$, remains unchanged. The surface albedo is 0.3 and the cosine of the solar illumination is $\mu_\odot = 0.7$.

It can be deduced from Fig. 3 that the linear perturbation theory yields satisfactory results for rather small perturbations. For larger perturbations the pure linear application turns out to be unsuitable. Therefore, the same atmosphere as in Fig. 2 is used to calculate two more base cases. These are located at the perturbation factors PF = 0.5 and 1.0. The result is shown in Fig. 4. The interpolation (shown as diamonds) improves the results dramatically. The errors of the pure linear perturbation theory, as depicted in Fig. 5 for each base case, is quite large whereas the error of the interpolated values is of the magnitude of tenths of a percent. A universal tool that automatically determines the positions of the base cases would be very desirable but has not been developed yet.

6.1.2. Perturbation of the phase function

The perturbation of the phase function is of special importance for three reasons. First, all orders of the expansion coefficient have to be taken into account for the calculation of the perturbation integral. Second, no interpolation will be carried out, although this might be possible in theory but would require a multivariate interpolation. Third, the first two reasons make the treatment of phase function perturbations

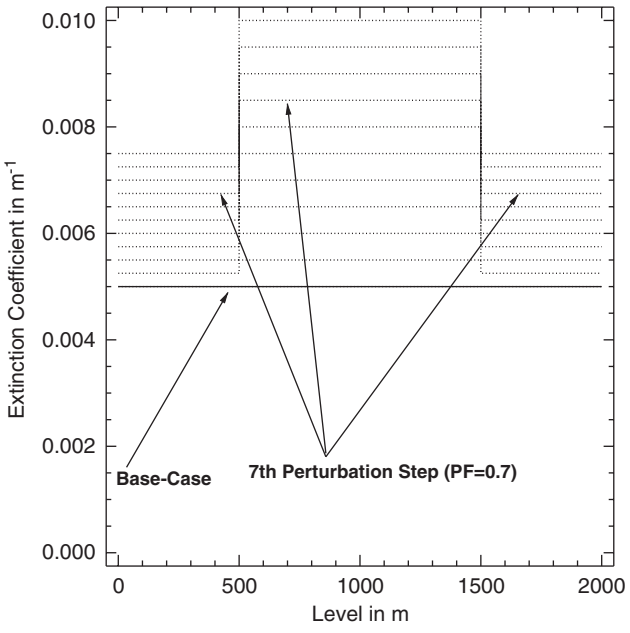

Fig. 2. Extinction/scattering coefficient variation as a function of height.

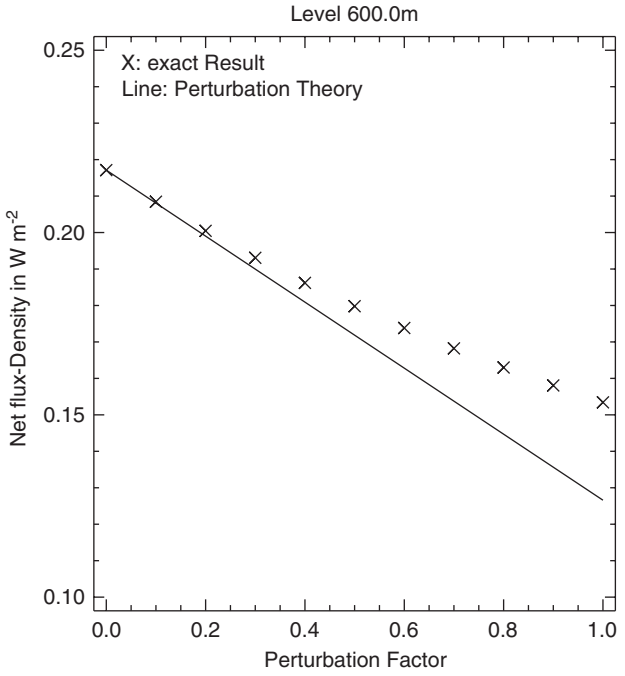

Fig. 3. Net flux in 600 m above ground as a function of the perturbation factor (PF). The "×" refer to exact results. "——" depicts the perturbation result.

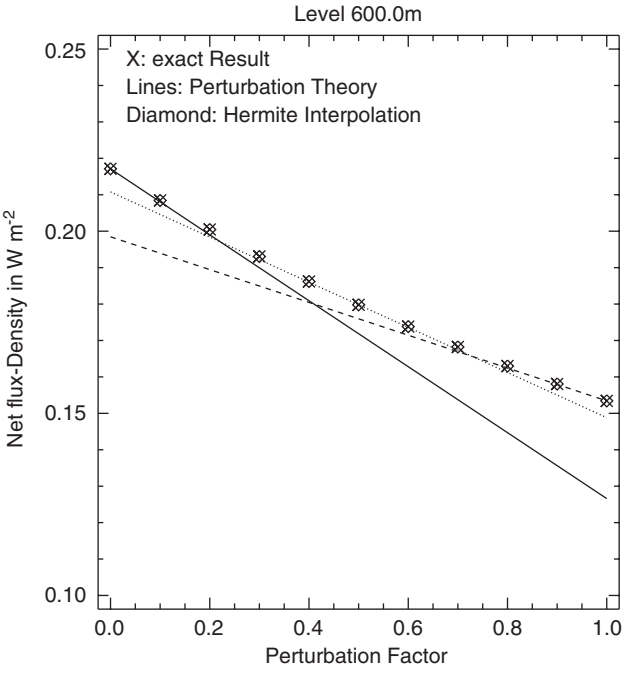

Fig. 4. Same as Fig. 3 but with multiple base cases and interpolated results shown. Base cases have been assigned to PF = 0, PF = 0.5 and PF = 1.

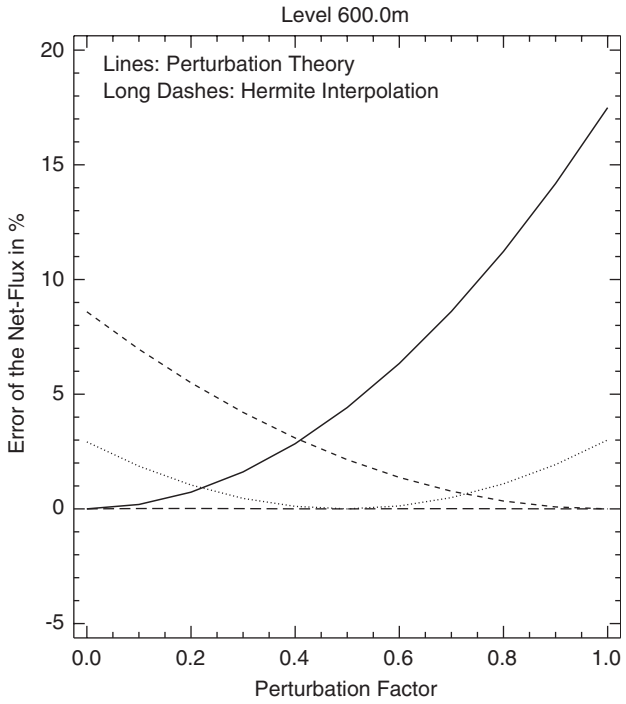

Fig. 5. Errors of the three base cases and the interpolation with respect to the exact results.

computationally expensive and at the same time the proper treatment of the phase function seems to be of special value given the wide range of scattering objects in the atmosphere.

As an example, the gradual transition of a HAZE-L phase function ($g = 0.8042$) into a C1 phase function ($g = 0.848$), see [15], is shown, see Fig. 6, thus describing the transformation of a smog or stratus layer into a cumulus cloud with otherwise the same optical properties. The scattering/extinction coefficient is $\sigma_t = 0.005\,\mathrm{m}^{-1}$, the remaining parameters are as before and no perturbation of the extinction/scattering coefficient is carried out. It can be seen that although two different cloud structures are underlying, the relation is close to the ideal linear case. The error for PF = 1.0 is just about 1%. That is not surprising as the asymmetry parameters are very close to each other.

Consider now the constant part of the phase function perturbation integral (Eq. (40)):

$$e_l = -\pi(2l+1)\int_0^{TOA} \mathrm{d}z\,\sigma_{s,b}(z)\xi_l^+(z)\xi_l(z).$$

In Fig. 7 the decline of e_l derived for the net-flux at the ground with increasing expansion order l is shown for both phase functions. It suggests that orders higher than four to five will not significantly contribute to the perturbation integral. Therefore, our choice of using only low order expansions does not seem to cause relevant errors.

The overall positive impression of the phase function perturbation changes considerably if very different phase functions are used and if significant perturbations of all optical properties occur at the same time. This will become of interest in the section about realistic cloud fields, see below.

6.2. Independent-pixel approximation results

In this paragraph, the RTPT will be applied to realistic clouds. The first one has multiple clear-sky areas, thus accounting for an inhomogeneous cloud field. The second cloud scene consists of several cumulus clouds whose optical depth can reach up to 100. The third one is a fairly stratified cloud with no clear sky areas and only slight horizontal variation.

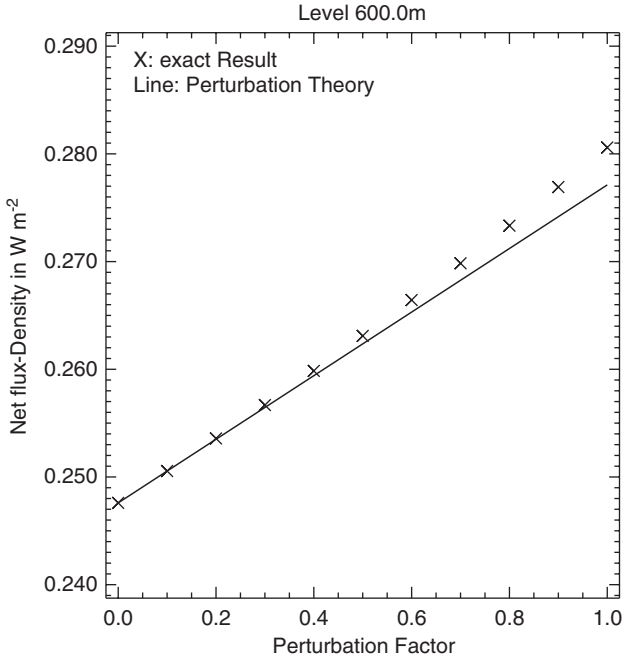

Fig. 6. Net flux in 600 m above ground as a function of the perturbation factor (PF) which refers here to a gradual transition in percent from the HAZE-L to the C1 phase function.

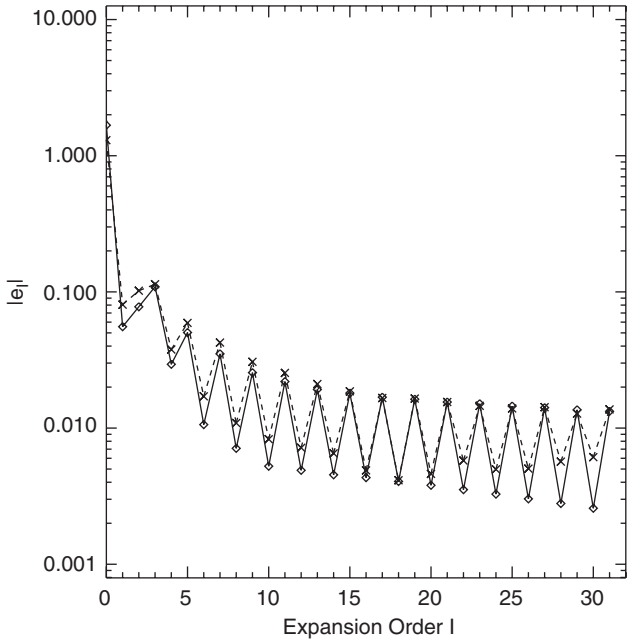

Fig. 7. Decline of the constant part of the phase function perturbation integral e_l with increasing l for $\mu_\odot = 1.0$, $\tau = 10$. The solid line refers to the Haze-L phase function, the dashed one to the C1 phase function.

6.2.1. *Broken stratocumulus from INSPECTRO data*

This stratocumulus cloud scene was created by incorporating realistic measurements acquired during the *INSPECTRO* campaign, see [16], into a cloud generator. The data have been made available to us by Kniffka,

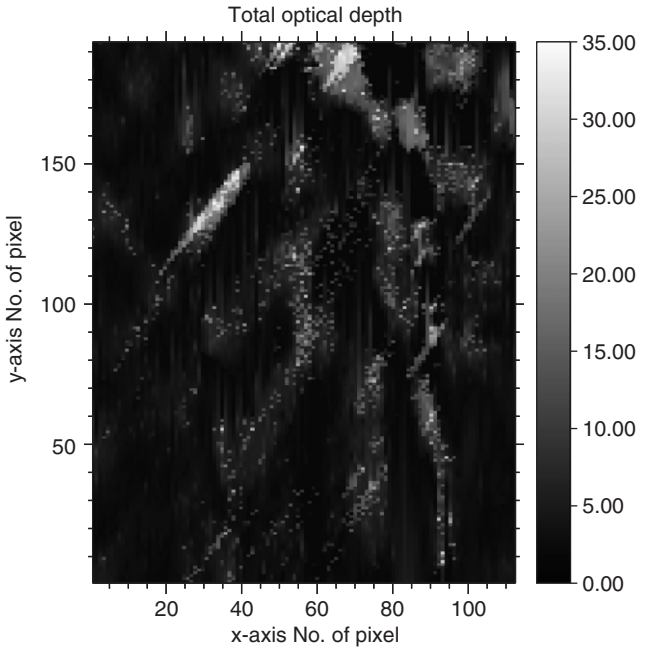

Fig. 8. Total optical depth of the Sc cloud field.

Table 1
Base case setup and phase functions for the Sc cloud: cl: cloud phase function, cs: clear-sky phase function

No.	Pixel (x, y)	Optical depth (approx.)	Phase function
1	(16, 1)	$\mathrm{Min}(\tau_t) = 0.14$	cs
2	(5, 172)	0.282	cs
3	(16, 40)	0.283	cl
4	(112, 155)	1.01	cl
5	(112, 132)	1.99	cl
6	(112, 160)	7.99	cl
7	(101, 132)	16.02	cl
8	(66, 189)	$\mathrm{Max}(\tau_t) = 34$	cl

Mayer and Scheirer. The resulting optical depth field for a wavelength of 550 nm is shown in Fig. 8. The scene is fairly inhomogeneous as large clear-sky areas with optical depths well below one lie in relative proximity of large optical depths of up to 34. The inhomogeneity refers not only to the horizontal directions but also to the vertical where strong gradients in the optical properties, namely the extinction coefficient, occur. The cloud itself is located between 1425 and 1725 m varying with position. The domain is $112 \times 193 \times 76$ grid points large and has a horizontal resolution of 200 m. The vertical resolution varies with height, being typically 75 m in the region of the cloud. A surface albedo of 8% was assumed and the direction of the sun was $\mu_\odot = 0.398$ and $\phi_\odot = 38.69^\circ$.

To enhance the results of the perturbation calculation and the Hermite interpolation, eight base cases with respect to the optical depth were chosen while two different phase functions were used at the same time, see Table 1. The two phase functions have been generated by averaging the expansion coefficients over the pixels which were, according to their optical depth, regarded as cloudy (cl) and cloud-free (cs), respectively. This way, seven intervals are spanned in which the Hermite interpolation can be applied. The accumulation of base cases at low optical depths accounts for the strong decline of the radiative field with increasing optical depth, especially in the case where absorption is present. For larger optical depths this relationship seems to saturate one way or another allowing for wider intervals. It has to be noted that the base cases are only chosen in a

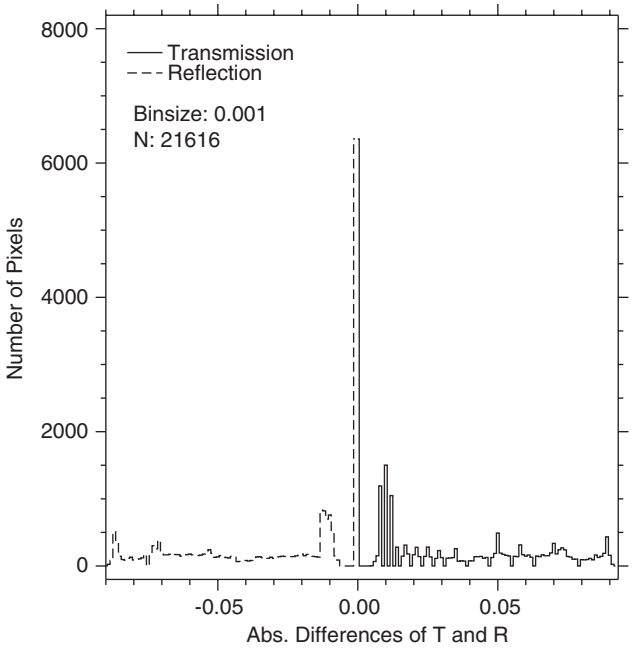

Fig. 9. Histogram of the absolute differences of transmission and reflection of all individual pixels for the Sc cloud.

semi-automatic manner. The first three and the last base case are selected according to the separation of the pixels in cloudy and clear sky, all other base cases are chosen at will. The fully automatic assignment of all base cases with appropriate pixels is yet to be achieved. Ways to reach this aim could comprise the straightforward allocation of a certain number of base cases to the given range of optical depths by analyzing the histogram of the optical depths or more sophisticated techniques like neural networks which could be trained to select the optimal pixels. To this end assembling a data base by carrying out numerous "training runs" beforehand would be most likely necessary. This selection of base cases would have to be carried out for each considered wavelength interval. However, it might also be possible to interpret differences of optical properties owing to their respective wavelength dependence as perturbations. As a result, the selection of base cases as well as the subsequent interpolation might be performed across wavelength intervals.

Because of the strong extinction we decided not to show relative errors, which would be rather large, but rather absolute differences. Before we explore the influence of the base cases we direct our attention to the distribution of the errors of transmission and reflection values of each pixel, respectively, to the absolute differences between exact computation and interpolated values of these two. Transmission and reflection (albedo) are defined here as

$$T = \frac{F_{\downarrow}(z=0)}{F_{\downarrow}(z=TOA)}, \quad R = \frac{F_{\uparrow}(z=TOA) - F_{\uparrow}(z=0)}{F_{\downarrow}(z=TOA)}. \tag{55}$$

In Fig. 9 the histogram of the absolute differences, gained by subtracting the interpolated results from the exact computation, of both are shown. One recognizes the sharp peaks at low absolute errors where most pixels are located in and which are accompanied by pixels with larger errors in the wings of the distributions.

In Fig. 10 the dependence of the absolute errors of T and R on the total optical depth are shown. In both graphs a wave-like structure is evident, yet the minima fail to approach zero error at all base case optical depths as the perturbation of the phase function is superimposed linearly. However, it is obvious from both graphs and the histograms that a striking symmetry exists where the transmitted light is systematically underestimated by the RTPT compared to the forward results while the reflected light is always overestimated.

In order to demonstrate the method's ability to yield vertical resolution the vertical profile of the mean intensity is shown in Fig. 11. One notes the good agreement of the RTPT profile with its forward counterpart, thus enabling the RTPT to efficiently derive actinic fluxes and heating rates as both are proportional to the

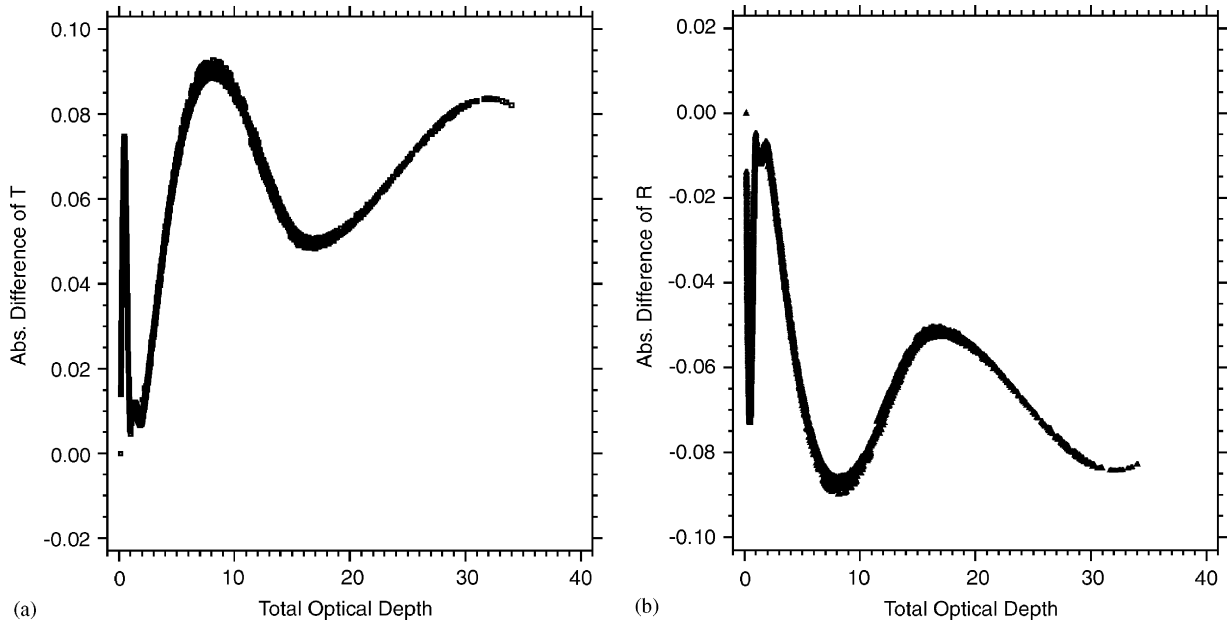

Fig. 10. ΔT and ΔR as a function of total optical depth of RTPT for the Sc cloud. (a) Absolute error of the transmission as a function of the total optical depth. (b) Absolute error of the albedo as a function of the total optical depth.

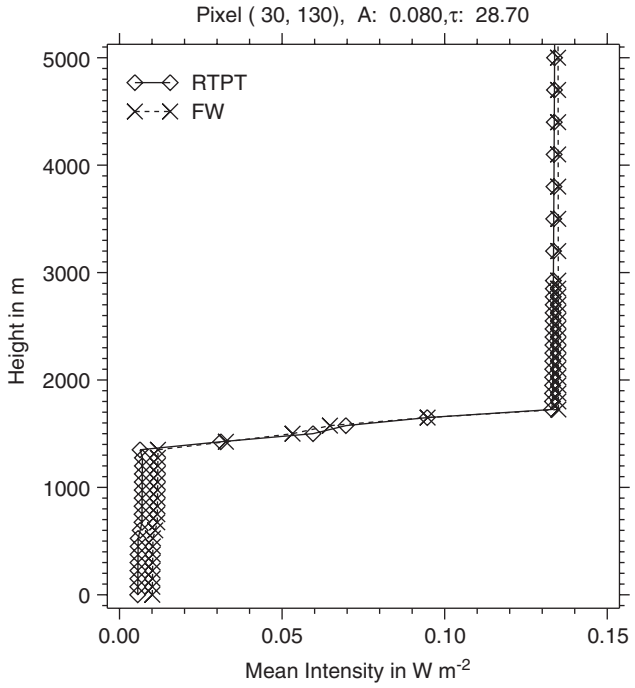

Fig. 11. Example for a vertical profile of the mean intensity in the Sc cloud derived by both methods.

mean intensity. Besides that, the implemented method is also able to derive up-, down-, and net flux-densities at all computational layer interfaces with reasonable accuracy.

Concerning the domain-averaged values we observe an error of $\Delta T = 6.8 \times 10^{-3}$ and $\Delta R = -5.84 \times 10^{-3}$.

At this place a remark about computational speed might be useful. The RTPT requires an adjoint solution at each vertical position where results are demanded for each effect and for every single base case. Thus, a

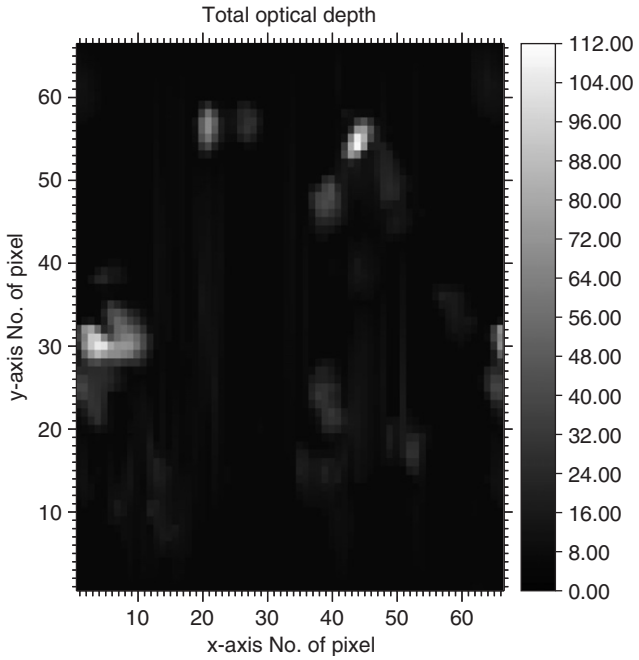

Fig. 12. Total optical depth of the *ARM* cumulus cloud field.

rather large number of combinations can arise. Therefore, it is not very meaningful to compute all effects at all vertical positions as that means that together with the lengthy computation of the phase function perturbation, which is required to be evaluated for each effect at those vertical positions in every pixel, the RTPT will take in fact longer than the forward model. However, the RTPT might offer some advantage if only few levels are selected. If three levels are chosen, here the top and bottom of the columns and additionally the level just below cloud-base which is referred to above, than the RTPT calculation is about four times faster than the forward calculation, although the selection of the base cases is not included in that figure and in turn no numerically optimized algorithm was developed. Generally speaking, it seems to make sense to use the approach the RTPT offers if only a limited number of output levels is considered to be important. A more specific estimation does not seem to be meaningful as the computational advantage over the forward calculation depends also on the number of pixels and effects.

6.2.2. Cumulus field from ARM data

This cumulus cloud field has been derived from measurements of the atmospheric radiation measurement (ARM) program, see [17], which have been preprocessed by a LES model and a cloud-generator, see [18]. The data have been provided to us by Victor Venema and Sebastián Gimeno García. The optical depth field for 330 nm is depicted in Fig. 12. The model domain has a size of $66 \times 66 \times 70$ grid points.

The horizontal resolution is 100 m and the vertical resolution in the region of the cloud is about 40 m. The cloud cover is only about 30% while the cloudy pixels can reach optical depths of over 100. Furthermore, the cloud is not limited to a flat layer but has also vertical structure and variation in shape. In Fig. 13 the horizontally (in x-direction) integrated optical depth is shown.

The overall setup for the calculations has not been changed, although the base cases have been adapted to the different distribution of total optical depths. The configuration is shown in Table 2. Due to the more inhomogeneously distributed cloud properties and the wider span of optical depths we use here 10 base cases with respect to the total optical depth. With regard to the phase function, the data consists of an asymmetry parameter for each cell. By employing the Henyey–Greenstein approximation higher orders of the phase function expansion are determined.

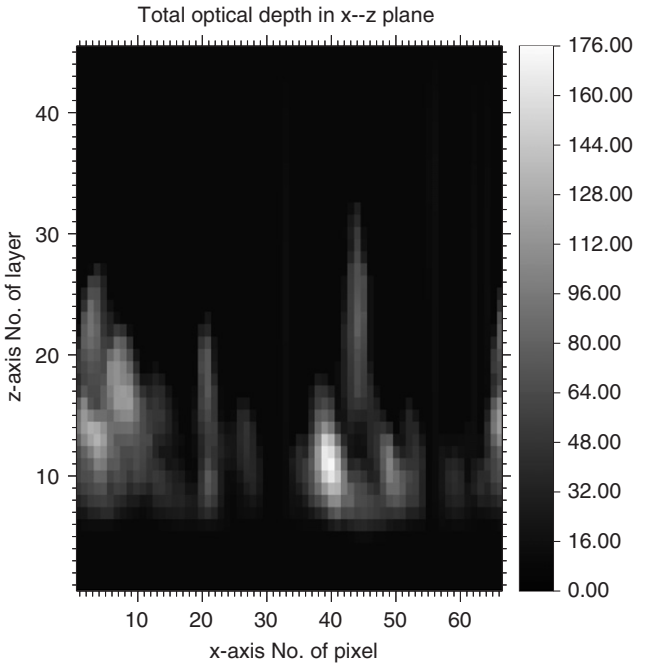

Fig. 13. x-integrated optical depth of the Cu cloud.

Table 2
Base case setup and phase functions for the Cu cloud : cl: cloud phase function, cs: clear-sky phase function

No.	Pixel (x, y)	Optical depth (approx.)	Phase function
1	(1, 1)	$\mathrm{Min}(\tau_t) = 0.13$	cs
2	(40, 59)	0.19	cs
3	(40, 29)	0.2	cl
4	(66, 63)	0.73	cl
5	(66, 58)	4.9	cl
6	(66, 61)	7.56	cl
7	(65, 23)	15.7	cl
8	(66, 24)	31.1	cl
9	(66, 31)	60.94	cl
10	(44, 54)	$\mathrm{Max}(\tau_t) = 106.4$	cl

The problem of over- and underestimation persists here and can become quite large according to the investigated position. This is to some extent reflected by the histograms of the individual errors of reflection and transmission of each pixel shown in Fig. 14. At first sight, the peaks are narrower than in the case before, although one has to consider that two more base cases have been used. But in the far left and right parts of the histogram, there is a considerable number of pixels where errors amount up to around 17%. That means by interpolating with respect to the total optical depth we cannot accurately account for strong internal variations between two columns. This problem was already addressed in Section 5. When the vertical distribution of the optical properties in a column which is treated by the interpolation technique considerably differs from the respective base case columns, the interpolation cannot adequately account for the perturbation. The linear treatment of the phase function perturbation adds to that problem as only two base cases with respect to the phase function perturbation are employed. Because of the ragged upper boundary of the cloud and the associated strong vertical gradients of optical properties, this defect is very prominent in the presented example. The next example contrast these features due its homogeneous cloud base and top. Here, the demand for columns which only differ due to a constant scaling is much better fulfilled.

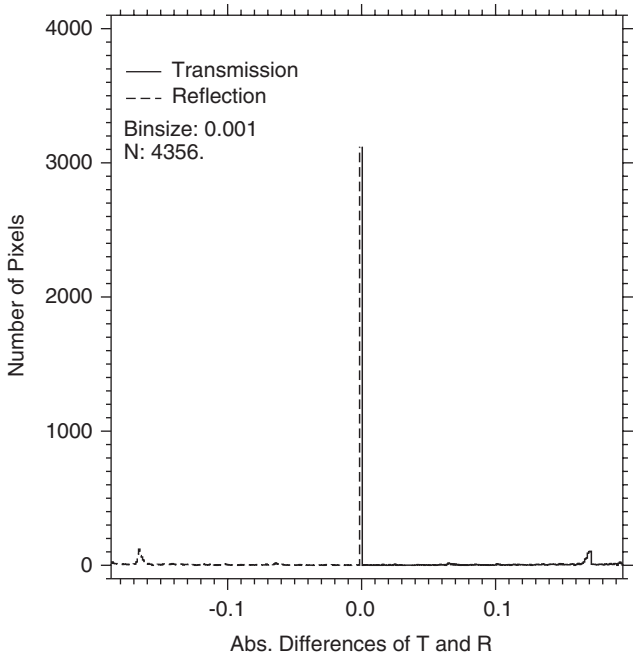

Fig. 14. Histogram of the absolute differences of transmission and reflection of all individual pixels for the Cu cloud.

For columns with optical depth identical to one of the base cases the interpolation approach is not suited. In this case the column will contain the results of the respective base case. The domain averaged absolute differences are $\Delta T = 3.95 \times 10^{-2}$ and $\Delta R = -3.84 \times 10^{-2}$. As the total number of pixels is too low in this case, we dispense with any acceleration comparisons as we do not expect the RTPT to have a significant advantage over the forward calculations.

6.2.3. *Stratus field from FIRE I data*

The last example is a stratus cloud which has been generated in an analogous manner as the cumulus field before. The data stems from the FIRE I campaign, see [19], and has been modeled by Duynkerke et al. [20]. See also [18]. The data were provided by Venema and Gimeno García. Because of its relatively moderate horizontal variability, it can be regarded as a counterpart to the cumulus field. The optical depth field for 330 nm is shown in Fig. 15. The vertical variation of the extinction coefficient is also very limited, especially the cloudbase and top height are practically constant. The horizontally integrated optical depth is shown in Fig. 16.

The cloud scene comprises $52 \times 52 \times 79$ grid points with a horizontal resolution of 50 m and a vertical resolution of 10 m in the relevant range. The remaining parameters are chosen as before. Accounting for the moderate perturbation of the optical parameters we have used only four base cases, see Table 3. As there are no clear-sky pixels both phase functions used for the base cases are nearly identical as well.

The relative neighborhood with respect to the total optical depth of base cases two and three has its origin in the semi-automatic way the bases-cases are chosen. Judging from the results of the stand-alone model two base cases would be sufficient for this cloud.

Over- and underestimation occurs in a more moderate fashion which can be obtained from Fig. 17 where the histograms are shown. The discussed symmetry is again present, yet not directly around zero error as the scene does not consist of clear sky areas but rather forms a local minimum at zero error. However, the errors of most of the pixels are confined to less than 1% while maximum values are less than 3%. This confirms the assumption that this effect is strongly related with the internal variation of the cloud and its shape. The domain averaged errors are $\Delta T = 3.95 \times 10^{-3}$ and $\Delta R = -4.88 \times 10^{-3}$.

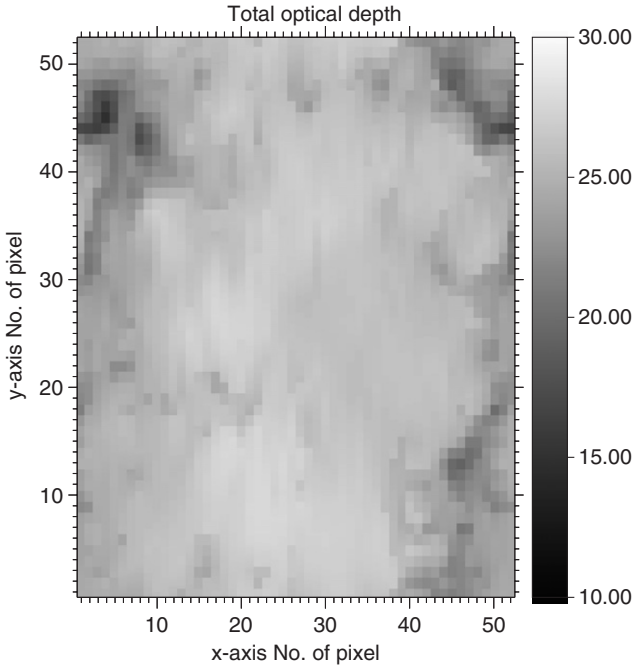

Fig. 15. Total optical depth of the *FIRE I* stratus cloud field.

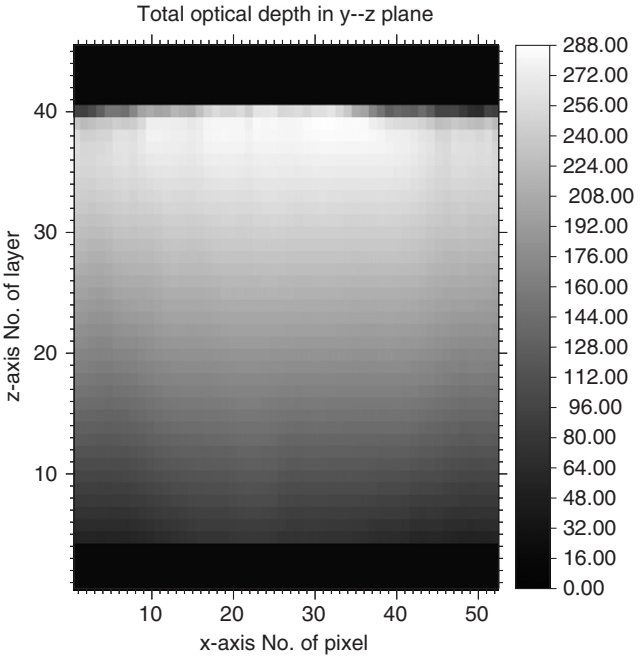

Fig. 16. Horizontal optical depth along the x-axis for the St cloud.

7. Conclusions

In this paper, we have presented an alternative way to deal with one-dimensional radiative transfer. To do so, we have shown the fundamental principles of the radiative transfer perturbation theory (RTPT) in

Table 3
Base case setup and phase functions for the St cloud: cl: cloud phase function

No.	Pixel (x, y)	Optical depth (approx.)	Phase function
1	(44, 3)	$\mathrm{Min}(\tau_t) = 14.98$	cl
2	(44, 49)	16.29	cl
3	(46, 5)	16.7	cl
4	(9, 22)	27.64	cl

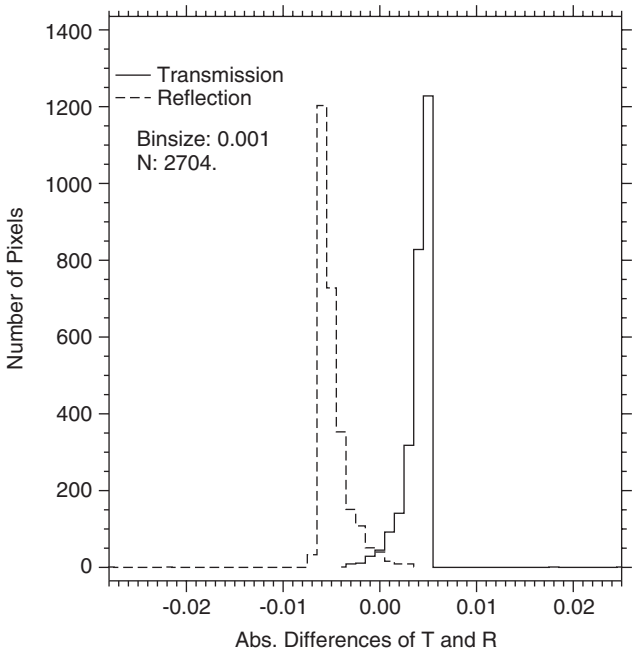

Fig. 17. Histogram of the absolute differences of transmission and reflection of all individual pixels for the St cloud.

combination with the Hermite interpolation and its utilization to cloud related independent-pixel radiative transfer computations. It was shown that, depending on the internal structure of the clouds, the deviations from usual forward independent-pixel calculations can become significant. This is especially true if fluxes inside the cloud are compared. The absolute errors of transmission and reflection of some pixels in the cumulus case can be as large as 17% whereas the domain averaged errors usually stay below 4%. In the course of our investigations, it also turned out that the RTPT can only speed up independent-pixel calculations if the problem allows to select only very few output levels. If results at all levels are demanded and if all sorts of perturbations have to be taken into account, meaning that all optical properties are subject to perturbations and the surface albedo has to be taken into account for each pixel, then the RTPT cannot offer an acceleration of the calculation. However, the RTPT could have an application in numerical weather prediction models. These models are usually equipped with two-stream models. In recent years numerical weather prediction models have been required to comprise more and more pixels due to the refinement of the spatial resolution. For numerical reasons the solution of the atmospheric equations requires a relatively small time step which is usually below 1 min depending of course on the spatial resolution. The time step for the radiation meaning the model time which elapses between two updates of the radiative field is much larger, typically around 1 h. A reduction of the radiation time step is for the practical feasibility of the model calculations nearly impossible. As a result, the computed heating/cooling rates are held constant until the next radiation time step. Thus, the RTPT could be run at just a few layer interfaces together with the usual forward calculation. Layer interfaces

regarded most important would be the top of atmosphere, the ground, the top of the atmospheric boundary layer and possibly the cloud base. The perturbation integrals determined that way could then be used to update the heating rates just by the presented interpolation and phase function perturbation. Additionally, the reflectance and transmission of each column could be easily calculated. Thus, one would gain at least the information crucial to energetically drive the dynamic part of the model. The required adaption of the RTPT to a two-stream model is possible and has been achieved by [4]. Nevertheless, another aspect of the perturbation theory is worth mentioning. As the respective perturbation integrals can be calculated independently of each other, it is possible to attribute a direct consequence in the observed change of the effect to each change in the optical properties. It has been demonstrated that the RTPT has significant potential for sensitivity studies, see Section 6.1. In addition to its didactic value, the RTPT can be recommended for use in the development and investigation of parameterizations and asymptotes of other radiative transfer techniques.

Acknowledgements

We would like to thank Dr. Ronald Scheirer and Dr. Bernhard Mayer of the Institute for Atmospheric Physics of the DLR for making available the cloud properties of the discussed cloud of the INSPECTRO campaign and Anke Kerstin Kniffka of the Institute for Meteorology of the University of Leipzig for providing us with the appropriate atmospheric and cloud optical properties. Thanks to Sebastián Gimeno García of the Institute of Meteorology of the University of Leipzig and to Dr. Victor Venema of the Meteorological Institute of the University of Bonn for supplying us with the optical parameters of the ARM and FIRE I clouds.

This work was funded by the German Federal Ministry of Education and Research (BMBF) under Grant 07 ATF 24-4 (4D Clouds).

Appendix A. The pseudo problem

The adjoint radiative transfer equation is

$$L^+ I^+ = Q^+ \tag{A.1}$$

with operator L^+:

$$L^+ := -\mu \frac{\partial}{\partial z} + \sigma_t(z) - \frac{\sigma_s(z)}{4\pi} \int_{4\pi} \mathrm{d}\Omega'\, p(z, \vec{\Omega}' \cdot \vec{\Omega}) \circ . \tag{A.2}$$

Define now

$$\Psi(z, -\vec{\Omega}) := I^+(z, \vec{\Omega}). \tag{A.3}$$

Insertion of Eq. (A.3) in (A.1) leads to

$$-\mu \frac{\partial \Psi(z, -\vec{\Omega})}{\partial z} + \sigma_t \Psi(z, -\vec{\Omega}) - \frac{\sigma_s}{4\pi} \int_{4\pi} \mathrm{d}\Omega'\, p(z, \vec{\Omega}' \cdot \vec{\Omega}) \Psi(z, -\vec{\Omega}') = Q^+(\Omega). \tag{A.4}$$

If the substitution $-\vec{\Omega} = \vec{\Omega}^*$, and hence $-\vec{\Omega}' = \vec{\Omega}'^*$ and $-\mu = \mu^*$, is introduced in Eq. (A.4), one yields

$$\mu \frac{\partial \Psi(z, \vec{\Omega}^*)}{\partial z} + \sigma_t \Psi(z, \vec{\Omega}^*) - \frac{\sigma_s}{4\pi} \int_{4\pi} \mathrm{d}\Omega'^*\, p(z, \vec{\Omega}'^* \cdot \vec{\Omega}^*) \Psi(z, \vec{\Omega}'^*) = Q^+(-\Omega^*), \tag{A.5}$$

where the identities $\mathrm{d}\Omega' = \mathrm{d}\Omega'^*$ and $-\vec{\Omega}'^* \cdot -\vec{\Omega}^* = \vec{\Omega}'^* \cdot \vec{\Omega}^*$ have been used. Note also that $\vec{\Omega} \cdot \vec{\Omega}' = \vec{\Omega}' \cdot \vec{\Omega}$ is valid as, due to the reciprocity of light, it can be assumed that for homogeneous scattering objects, the scattering phase function rather depends on the scattering angle in a relative description than in absolute terms. The right-hand side of Eq. (A.5) has the same structure as the usual forward radiative transfer equation. Thus, Eq. (A.5) can be written as

$$L\Psi(z, \vec{\Omega}) = Q^+(z, -\vec{\Omega}). \tag{A.6}$$

As a result, if the boundary conditions for the forward problem are applied, Eq. (A.6) can be used to calculate I^+ by means of the substitution (A.3). This requires only the adaption of the employed standard algorithm to the new source $Q^+(z,-\vec{\Omega})$ and no new radiative transfer model has to be established.

Appendix B. First order perturbation expansion

The derivation of the linear perturbation formula after Ustinov [7] is briefly addressed. The basic equations are restated as

$$LI = Q, \tag{B.1}$$

$$L_\mathrm{b} I_\mathrm{b} = Q_\mathrm{b}, \tag{B.2}$$

$$L_\mathrm{b}^+ I_\mathrm{b}^+ = R. \tag{B.3}$$

Multiplying (B.3) by I_b and multiplying (B.2) by I_b^+ leads to

$$I_\mathrm{b} L_\mathrm{b}^+ I_\mathrm{b}^+ = R I_\mathrm{b}, \tag{B.4}$$

$$I_\mathrm{b}^+ L_\mathrm{b} I_\mathrm{b} = Q_\mathrm{b} I_\mathrm{b}^+. \tag{B.5}$$

Subtracting (B.5) from (B.4) and applying the phase space integral $\langle\cdot,\cdot\rangle$ leads to

$$E_\mathrm{b} = \langle Q_\mathrm{b}, I_\mathrm{b}^+\rangle - \langle I_\mathrm{b}^+, L_\mathrm{b} I_\mathrm{b}\rangle + \langle I_\mathrm{b}, L_\mathrm{b}^+ I_\mathrm{b}^+\rangle. \tag{B.6}$$

Multiplying now (B.3) by I and multiplying (B.1) by I_b^+ leads to

$$I L_\mathrm{b}^+ I_\mathrm{b}^+ = R I, \tag{B.7}$$

$$I_\mathrm{b}^+ L I = Q I_\mathrm{b}^+. \tag{B.8}$$

Subtraction of (B.8) from (B.7) and integration leads to

$$E = \langle Q, I_\mathrm{b}^+\rangle - \langle I_\mathrm{b}^+, L I\rangle + \langle I, L_\mathrm{b}^+ I_\mathrm{b}^+\rangle. \tag{B.9}$$

Finally

$$E - E_\mathrm{b} = \Delta E = \langle I_\mathrm{b}^+, \Delta Q - \Delta L I_\mathrm{b}\rangle \tag{B.10}$$

with

$$\begin{aligned} \Delta Q &= Q - Q_\mathrm{b}, \\ \Delta L &= L - L_\mathrm{b}. \end{aligned} \tag{B.11}$$

References

[1] Bell GI, Glasstone S. Nuclear reactor theory. New York: Van Nostrand Reinhold; 1970.

[2] Marchuk GI. Equation for the value of information from weather satellites and formulation of inverse problems. Cosmic Res 1964;2:394–409.

[3] Box MA, Gerstl SAW, Simmer C. Application of the adjoint formulation to the calculation of atmospheric radiative effects. Contr Atmos Phys 1988;61:303–11.

[4] Gabriel P, Harrington J, Stephens GL, Schneider T. Adjoint perturbation method applied to two-stream radiative transfer. JQSRT 1998;59:1–24.

[5] Gabriel P, Stephens GL, Wittmeyer IL. Adjoint perturbation and selection rule method for solar broadband two-stream fluxes in multi-layer media. JQSRT 2000;65:693–728.

[6] Stamnes K, Tsay SC, Wiscombe W, Jayaweera K. Numerically stable algorithm for discrete-ordinate-method radiative transfer in multiple scattering and emitting layered media. Appl Opt 1988;27:2502–9.

[7] Ustinov EA. Inverse problem of the photometry of the solar radiation reflected by an optically thick planetary atmosphere: mathematical framework and weighting functions of the linearized inverse problem. Cosmic Res 1991;29:519–32.

[8] Box MA, Gerstl SAW, Simmer C. Computation of atmospheric radiative effects via perturbation theory. Contr Atmos Phys 1989;62:193–9.
[9] Walter HH, Landgraf J, Hasekamp OP. Linearization of a pseudo-spherical vector radiative transfer model. JQSRT 2004;85:251–83.
[10] Landgraf J, Hasekamp OP, Trautmann T. Linearization of radiative transfer with respect to surface properties. JQSRT 2002;72:327–39.
[11] Muldashev TZ, Lyapustin AI, Sultangazin UM. Spherical harmonics method in the problem of radiative transfer in the atmosphere-surface system. JQSRT 1999;61:393–404.
[12] Liou KN. An introduction to atmospheric radiation, 2nd ed. New York: Academic Press; 2002.
[13] Kahaner D, Moler C, Nash S. Numerical methods and software. Englewood Cliffs, NJ: Prentice-Hall; 1989.
[14] Maess G. Vorlesungen über numerische Mathematik. Basel: Birkhäuser Verlag; 1988.
[15] Garcia RDM, Siewert CE. Benchmark results in radiative transfer. Trans Theory Statist Phys 1985;14:437–83.
[16] INSPECTRO Webpage; 2002. http://imk-ifu.fzk.de/inspectro/
[17] ARM Webpage; 2004. http://www.arm.gov
[18] Venema V, Meyer S, GarcÃa SG, Kniffka A, Simmer C, Crewell S, et al. Surrogate cloud fields generated with the iterative amplitude adapted Fourier transform algorithm. Tellus A 2006;58:104–20.
[19] FIRE I Webpage; 2002. http://asd-www.larc.nasa.gov/fire/fire1.html
[20] Duynkerke PG, d Roode SR, v Zanten MC, Calvo J, Cuxart J, Cheinet S, et al. Observations and numerical simulations of the diurnal cycle of the EUROCS stratocumulus case. Quart J R Met Soc 2004;130:3245–68.